photonics

MDPI

Article

An Integrated Acquisition and Retrieval System for Atmospheric LiDAR

Ruixin Gui [1,2], Chenbo Xie [2,*], Jie Lu [1,2], Zichen Zhang [2] and Ruhang Zhang [1,2]

[1] Science Island Branch of Graduate School, University of Science and Technology of China, Hefei 230026, China; rxgui@mail.ustc.edu.cn (R.G.); ean@mail.ustc.edu.cn (J.L.); zhang.rh@mail.ustc.edu.cn (R.Z.)
[2] State Key Laboratory of Laser Interaction with Matter, Anhui Institute of Optics and Fine Mechanics, Hefei Institutes of Physical Science, Chinese Academy of Sciences, Hefei 230031, China; efzhangzichen@gmail.com
* Correspondence: cbxie@aiofm.ac.cn; Tel.: +86-189-5516-4393

Abstract

An integrated acquisition and on-board retrieval system was developed for aerosol extinction measurements with a 532 nm atmospheric lidar. The system combines analog echo acquisition, pulse accumulation, and Fernald-type retrieval within the instrument. At a laser repetition rate of 3 kHz, the programmable logic of a Zynq system-on-chip accumulates 3000 echo records into one 4000-bin profile per second, with a range-bin spacing of 7.5 m. Coordinated profile handover and task scheduling allow the processor to retrieve one profile while acquisition and accumulation continue. The retrieval implementation reuses fixed coefficients and reorganizes calculations while preserving the order of cumulative integration. Embedded processing of a measured profile, including reference selection, took 12.49 ms, compared with the 1 s interval between accumulated profiles. For the same profile, the maximum absolute difference from a desktop C build of the same retrieval code was 2.384×10^{-7} km^{-1} at matched valid range bins. The system was also used in a 60 h horizontal field campaign to record the temporal evolution of range-resolved atmospheric extinction.

Keywords: atmospheric lidar; aerosol extinction; integrated acquisition and retrieval; embedded processing; Fernald inversion; Zynq system-on-chip

1. Introduction

Atmospheric lidar provides range-resolved measurements for studying aerosol distributions and transport [1]. Compact depolarization lidars have been used to retrieve aerosol optical properties during mobile observations [2] and to follow their temporal evolution at a fixed site [3]. Scanning Mie lidar has also been used to track near-surface aerosol plumes [4]. These observations require coordinated acquisition, instrument control, and data processing. In high-repetition-rate systems, echoes from successive laser pulses are accumulated to form a measurement profile [5]. Acquisition therefore follows individual laser triggers, whereas retrieval operates on completed profiles.

System-on-chip (SoC) platforms have been used to combine acquisition, control, and preprocessing in atmospheric lidar. Reported Zynq systems accumulate photon-counting data in programmable logic (PL), while the ARM processing system (PS) handles preprocessing, control, and storage [5,6]. The Small Mobile Ozone Lidar also uses a Zynq SoC for data acquisition and instrument automation [7].

The allocation of further processing tasks depends on the lidar measurement. In coherent Doppler lidar, spectral processing on a field-programmable gate array (FPGA) has been

Check for updates

Received: 30 October 2026
Revised: 16 November 2026
Accepted: 19 November 2026
Published: 23 November 2026

Copyright: © 2026 by the authors. Licensee MDPI, Basel, Switzerland. This article is an open access article distributed under the terms and conditions of the Creative Commons Attribution (CC BY) license.

combined with host-side wind estimation [8]. Other systems use edge classifiers to decide which Doppler-lidar spectra to retain [9]. Kim et al. studied shared-memory coordination between two ARM cores for scanning lidar using hardware-in-the-loop emulation [10]. Table 1 compares the processing tasks and evaluation settings of these systems.

The present work addresses on-board aerosol extinction retrieval from an analog channel during ongoing acquisition. At the selected acquisition settings, a new accumulated profile becomes available every second. The processor must retain a complete input while the next profile is acquired and accumulated. Its processing time must also fit within that interval to sustain the output rate.

Table 1. Processing tasks and evaluation settings of selected embedded and edge-processing lidar systems.

Study	Task and Platform	Processing Arrangement	Evaluation
Cheng et al. (2022) [5]	Photon-counting atmospheric lidar; Zynq SoC	PL counting and accumulation; ARM background removal, control, and storage	Counter comparison and atmospheric observations
Cheng and Xie (2023) [6]	High-repetition-rate photon-counting lidar; Zynq-7020	Accumulation and AXI-to-DDR transfer; ARM preprocessing and storage	Acquisition comparisons and field observations
Liu et al. (2023) [8]	Coherent Doppler wind lidar; Kintex-7 and host	FPGA sampling and spectra; host-side velocity estimation	24 h observations and wind comparisons
Jackson et al. (2023) [9]	Doppler-lidar classification; Xavier NX edge node	Classifiers guide retention of spectral data	Doppler-lidar observations from the Atmospheric Radiation Measurement facility
Chouza et al. (2025) [7]	Mobile ozone lidar; Zynq-7010	Acquisition and automation on SoC; GLASS retrieval location unspecified	Airborne and in situ comparisons
Kim et al. (2025) [10]	Scanning time-of-flight lidar; dual-core Zynq-7020	Shared-memory coordination of tasks on two ARM cores	Hardware-in-the-loop emulation
This work	Acquisition and aerosol extinction; Zynq-7020	PL waveform accumulation; ARM extinction retrieval from completed profiles	Numerical comparisons, processor timing, and atmospheric observations

Here, we extend on-board processing to aerosol extinction retrieval by combining PL acquisition and accumulation with ARM processing of completed profiles. Profile handover and task scheduling allow these stages to operate concurrently, so the instrument produces extinction profiles while new echoes are acquired. Retrieval parameters can be adjusted without changing the acquisition logic. Coefficient reuse and computation reorganization reduce the processing workload while preserving the integration order. Numerical comparisons, processor timing, and field observations evaluate the implementation and its sustained operation.

2. System Architecture and Hardware Design

2.1. LiDAR System Overview

Figure 1 shows the optical front end and the custom acquisition and processing board built around a Zynq-7000 SoC (XC7Z020; Xilinx, Inc., San Jose, CA, USA) The board supports analog waveform acquisition and photon counting; the configuration studied here uses one analog channel connected to a photomultiplier tube (PMT). The acquisition settings in Table 2 give a 200 µs sampling window per pulse and one accumulated profile per second.

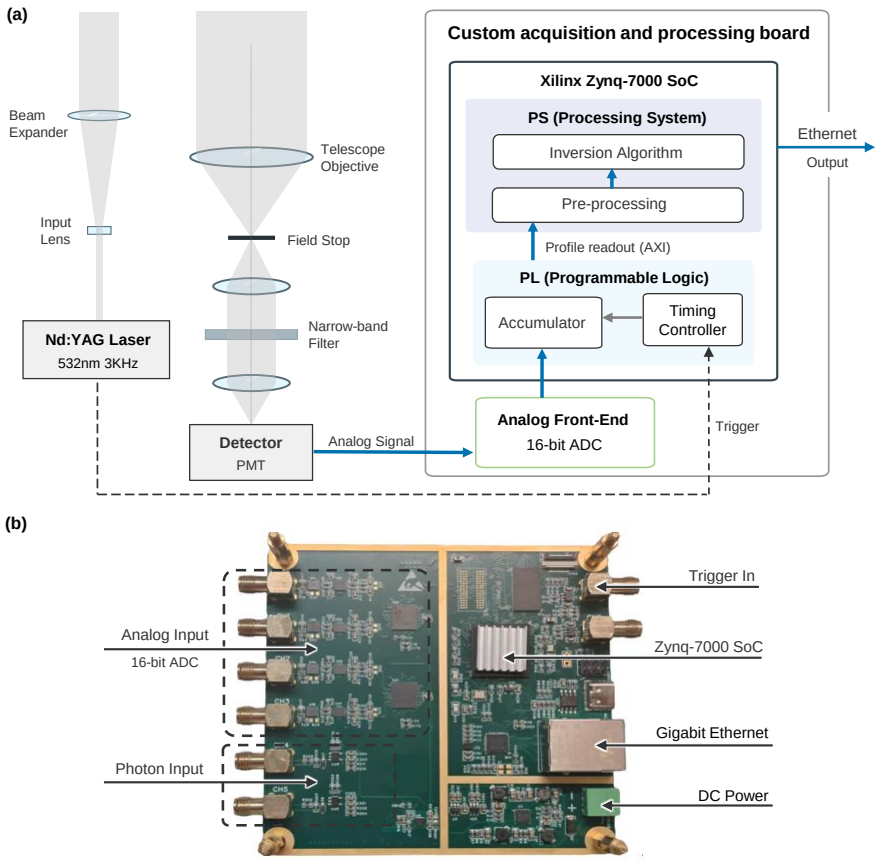


Figure 1. System overview. (**a**) Optical front end and the analog acquisition–retrieval path from the PMT signal to the extinction profile on the Zynq board. The PL handles pulse accumulation and timing control, while the PS performs preprocessing and extinction retrieval. Results are sent over Ethernet. (**b**) Photograph of the acquisition and processing board.

Table 2. Instrument parameters and single-channel acquisition settings.

Parameter	Value
Laser wavelength/pulse energy	532 nm/200 μJ
Pulse repetition rate	3 kHz
Laser pulse duration (manufacturer specification)	<15 ns
Beam divergence	<0.5 mrad
Receiver telescope aperture	25 mm
Filter central wavelength/FWHM	532 nm/1 nm
Receiver field of view	1 mrad
Detector	Hamamatsu H10721P-210 PMT
Typical PMT rise time (datasheet)	0.57 ns
SoC	Xilinx Zynq-7000 (XC7Z020)
Analog sampling	16 bit, 20 MSPS
Range-bin spacing/Samples per pulse, N_{bin}	7.5 m/4000
Board-level power	Approximately 5.2 W

The transmitter is a Nd:YAG laser operating at 532 nm with a pulse repetition rate of 3 kHz. In the bistatic arrangement shown in Figure 1a, the receiver collects backscattered light through a telescope, a field stop, and a narrow-band filter. The received light is detected by a H10721P-210 PMT module (Hamamatsu Photonics K.K., Hamamatsu, Shizuoka, Japan) whose analog current output is connected to the acquisition board.

The PMT output is connected to a 50 Ω input without additional voltage amplification and digitized by a 16-bit analog-to-digital converter (ADC) at 20 MSPS. The configured differential input range is ±1 V. The ADC datasheet specifies a typical full-power sample-and-hold bandwidth of 550 MHz.

The laser synchronization signal provides the timing reference for each acquisition window. The PL applies the same sampling sequence to successive pulses so that samples with matching indices can be accumulated. The 4000-sample acquisition window lasts 200 µs, within the approximately 333 µs interval between laser pulses. Accumulating 3000 pulses produces one profile per second, as summarized in Table 2. The 7.5 m range-bin spacing follows from the 50 ns sampling interval at 20 MSPS.

The PL accumulates echoes in working RAM and writes the completed bin sums to output BRAM. The PS reads these profiles through the AXI BRAM controller and copies them into DDR. Section 2.3 describes the timing and buffer reuse conditions.

The PS performs preprocessing followed by Fernald-type extinction retrieval. The host configures the instrument and collects, stores, and displays results received over Ethernet.

2.2. Hardware Implementation and Resources

The custom acquisition module deserializes the ADC output, aligns the samples, and accumulates successive echoes. The acquisition logic operates at 160 MHz, while the ADC samples at 20 MSPS. On-chip block RAM (BRAM) provides separate storage for running sums and completed profiles. The PS reads completed profiles through an Advanced eXtensible Interface (AXI) BRAM controller and copies them into on-board double-data-rate (DDR) memory.

Table 3 summarizes resource use, routed timing, and estimated on-chip power for the complete hardware design, including the additional acquisition interfaces. The routed design has positive worst setup and hold slacks under the applied timing constraints. The 1.623 W value is the Vivado on-chip estimate for the implemented Zynq design. Board-level power was approximately 5.2 W under full operation, calculated from the measured voltage and current at the board supply input. This measurement includes the analog front end, Zynq device, memory, Ethernet circuitry, and board power conversion, but excludes the external laser and other separately powered lidar components.

Table 3. Post-implementation PL resource, timing, and power summary.

Item	Used	Available	Util.
Slice LUTs	8182	53,200	15.38%
Slice registers	9694	106,400	9.11%
Block RAM tiles	69.5	140	49.64%
DSP48E1	2	220	0.91%
WNS	0.332 ns		
TNS	0 ns		
WHS	0.046 ns		
Vivado on-chip power	1.623 W (implementation estimate)		

2.3. Profile Handover and Concurrent Processing

Figure 2a shows the PL accumulating profile $K + 1$ while the PS processes profile K. In Figure 2b, working RAM holds running sums, output BRAM holds the completed profile, and DDR buffers hold software inputs and results.

The first pulse of each profile initializes the running sums in working RAM; subsequent pulses update them bin by bin. During the final pulse, each completed bin sum is

written to output BRAM. Signed 32-bit accumulation accommodates the sum of 3000 signed 16-bit samples.

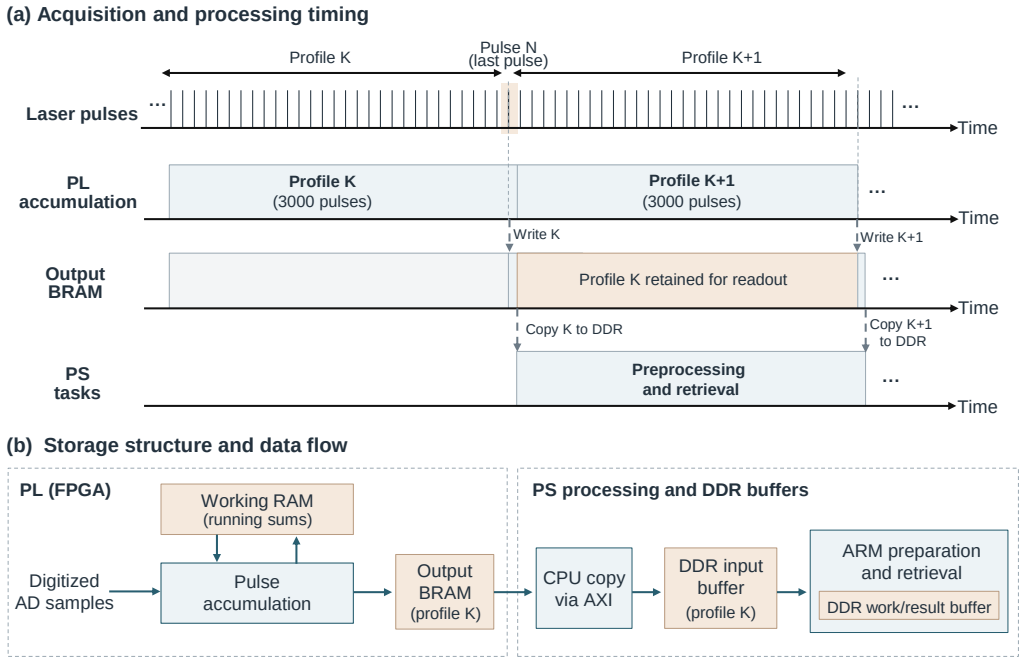


Figure 2. Acquisition and retrieval on the same board. (**a**) Timing of laser pulses, PL accumulation, output BRAM updates, and PS processing for $N = 3000$ pulses per profile. The PS copies a profile after its final BRAM write and processes the DDR copy while acquisition continues. Pulse markers and task bars indicate the sequence of operations, not measured durations. (**b**) Data flow from pulse accumulation through output BRAM to the DDR input and work/result buffers.

The PL and PS access output BRAM through separate ports. Under FreeRTOS, a PL interrupt notifies the readout task, which has higher priority than input preparation and retrieval. Copying begins after the final BRAM write and must finish before the next completed profile starts overwriting this storage. After copying, input preparation and retrieval use the DDR data while the PL continues acquisition.

Two DDR input buffers and two DDR work/result buffers separate profile readout from retrieval and result collection. An input buffer is released after its data have been converted to a floating-point copy in a work/result buffer. The processor performs retrieval using this copy and retains the result until the host acknowledges its identifier. If no buffer is available, the software records an overrun or a discarded processing window.

Readout selects the configured analog channel and applies the detector polarity. The accumulated samples are then converted to floating-point ADC-count values for the preprocessing and extinction retrieval described in Section 3.

3. Single-Channel Retrieval and ARM Implementation

3.1. Preprocessing and Reference Selection

Each retrieval call processes one accumulated analog profile from the DDR input buffer, without averaging successive profiles. The range grid is $r_i = (i + 1)\Delta r$, for $i = 0, \ldots, 3999$, with $\Delta r = 0.0075$ km. Figure 3 shows the three processing stages.

For each accumulated profile, the last 600 bins, spanning approximately 25.51–30.00 km, are used to estimate the background under the assumption of negligible atmospheric return. Their mean is subtracted before range-domain smoothing. A normalized, symmetric seven-point Gaussian kernel then smooths the centered signal along range. The first and last

three bins remain unfiltered. The mean and standard deviation over the same 600 bins after smoothing define the residual background B and noise estimate σ_B, with the variance averaged over all 600 bins. The net signal P_i and range-corrected signal X_i are

$$P_i = \widetilde{P}_i - B, \qquad X_i = P_i r_i^2, \tag{1}$$

Here, $\widetilde{P}_i$ is the smoothed, offset-corrected signal, and the signal-to-noise ratio (SNR) used for screening is P_i/σ_B. Non-positive or non-finite P_i values are excluded before logarithmic fitting; the SNR must also be finite.

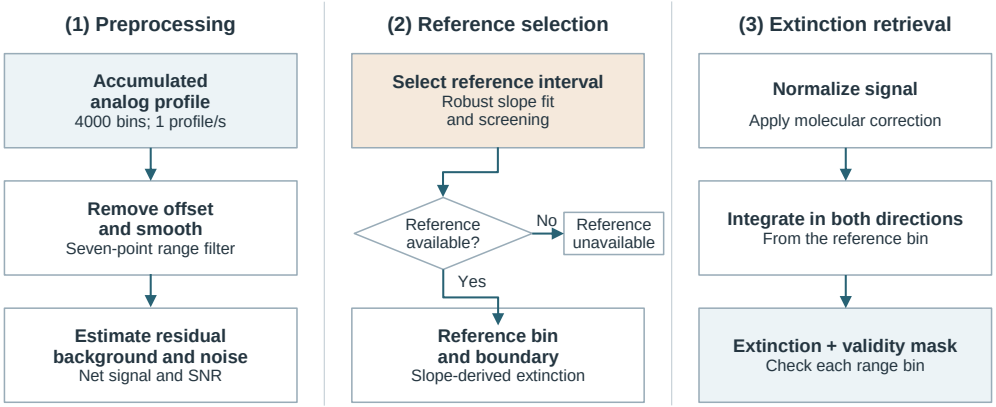


Figure 3. Single-channel aerosol extinction retrieval. A completed analog profile passes through preprocessing, reference selection, and Fernald inversion. Reference selection estimates a boundary value from the fitted slope and applies a fallback search if needed. Retrieval proceeds from the selected reference bin toward shorter and longer ranges, producing extinction values and a per-bin validity mask.

For each profile, candidate reference intervals between 1 and 7.5 km are examined using 201-bin windows stepped by 25 bins. Within each window, $\ln X_i = ar_i + b$ is fitted using iteratively reweighted least squares. Primary screening requires a negative slope, a median SNR of at least 5, and $R^2 \geq 0.95$. Candidate extinction estimates are also checked for consistency. The farthest retained interval provides the reference bin i_{ref} and the aerosol extinction estimate

$$\alpha_{a,\mathrm{ref}} = -\frac{a}{2} - \alpha_m. \tag{2}$$

This estimate assumes an approximately homogeneous, fully overlapped reference interval along range, so that the backscatter gradient contributes little to the fitted slope [11,12]. A fallback search uses a continuous high-SNR interval when the primary search does not return a reference. If neither search succeeds, the module reports a reference-selection failure.

3.2. Discrete Extinction Retrieval

Aerosol extinction is retrieved using a discrete form of the Fernald inversion with separate aerosol and molecular lidar ratios [13,14]. Let $\eta = S_a/S_m$. For the horizontal configuration, the molecular extinction α_m is taken as constant. The implementation uses $S_a = 50$ sr, $S_m = 8\pi/3$ sr, and $\alpha_m = 0.01$ km^{-1}. The aerosol lidar ratio is prescribed empirically, and the molecular extinction is held fixed; neither was independently measured during the campaign. The molecular correction M_i and reference-normalized signal y_i are

$$\begin{aligned} M_i &= \exp[2(\eta - 1)\alpha_m r_i], \\ y_i &= \frac{X_i/M_i}{X_{i_{\mathrm{ref}}}/M_{i_{\mathrm{ref}}}}. \end{aligned} \tag{3}$$

Thus $y_{i_{\mathrm{ref}}} = 1$, and the reference denominator is

$$c = \frac{1}{\alpha_{a,\mathrm{ref}} + \eta\alpha_m}. \tag{4}$$

Trapezoidal integration proceeds from the reference bin toward shorter and longer ranges:

$$I_i = \begin{cases} \dfrac{\Delta r}{2} \displaystyle\sum_{k=i}^{i_{\mathrm{ref}}-1} (y_k + y_{k+1}), & i < i_{\mathrm{ref}}, \\ 0, & i = i_{\mathrm{ref}}, \\ \dfrac{\Delta r}{2} \displaystyle\sum_{k=i_{\mathrm{ref}}+1}^{i} (y_k + y_{k-1}), & i > i_{\mathrm{ref}}. \end{cases} \tag{5}$$

The denominator D_i and aerosol extinction $\alpha_a[i]$ are then

$$D_i = \begin{cases} c + 2I_i, & i < i_{\mathrm{ref}}, \\ c, & i = i_{\mathrm{ref}}, \\ c - 2I_i, & i > i_{\mathrm{ref}}, \end{cases} \qquad \alpha_a[i] = \frac{y_i}{D_i} - \eta\alpha_m. \tag{6}$$

The extinction is expressed in km^{-1}. Numerical evaluation requires finite $y_i > 0$ and a finite denominator $D_i \geq 0.40c$ that can be represented as a positive single-precision value. A failed numerical check produces NaN. The validity mask additionally requires finite extinction and SNR, SNR ≥ 3, and the processing cutoff $r_i \geq 0.15$ km. Bins rejected only by the SNR or range criteria retain their computed values with the mask unset. Finite negative extinction estimates are not clipped.

3.3. Computation Organization on the ARM Processor

The computation is organized around quantities shared by successive profiles and the ordering required by integration (Figure 4). For a fixed range grid and fixed model parameters, the coefficients

$$q_i = r_i^2 \exp[-2(\eta - 1)\alpha_m r_i] \tag{7}$$

are precomputed and stored once for each range bin. For each new profile, Equation (3) becomes $y_i = (P_i q_i)/(P_{i_{\mathrm{ref}}} q_{i_{\mathrm{ref}}})$. This replaces per-profile range and molecular-factor evaluation with multiplication and reference-point normalization. The table is rebuilt when the range grid or model parameters change.

In reference fitting, an order-statistic selection routine obtains the medians needed for the residual center and scale, with sorting retained as a fallback. Weight evaluation assigns unity directly when $d_i \leq t$ and computes t/d_i only for larger deviations [Figure 4b]. These changes reduce sorting and division work while retaining the fitting and candidate-selection rules.

The cumulative integral is evaluated sequentially from the reference bin in each range direction. Within each group of eight bins, denominators are formed in traversal order before extinction and validity are evaluated for those bins [Figure 4c]. The running sum carries over between groups; any final group with fewer than eight bins is processed individually. The group size was selected by measurements on the target processor.

Profile arrays, coefficient tables, and point-wise output arithmetic use single precision. Background statistics, reference fitting, and cumulative integration use double precision. Each denominator is converted to single precision for the final division, and working arrays are reused across profiles. Section 4 evaluates numerical agreement and processing time; full-algorithm timing includes reference selection.

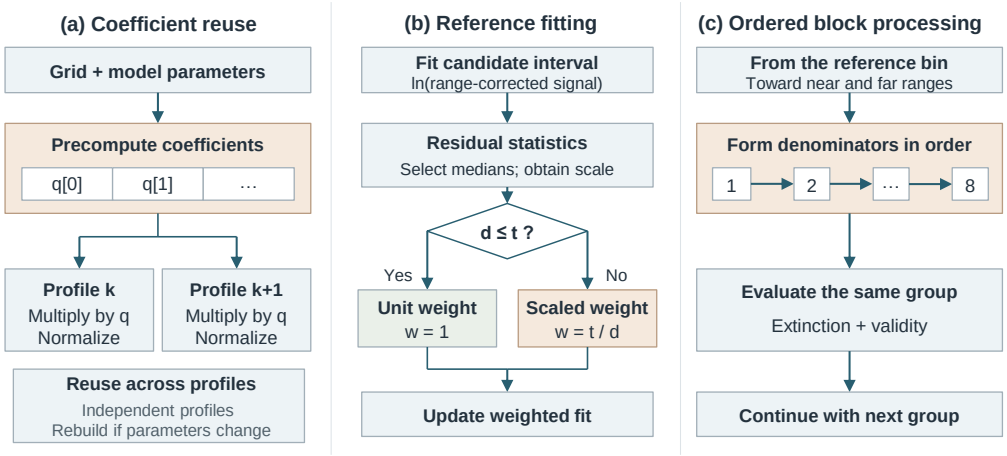


Figure 4. Computation organization on the ARM processor. (**a**) A fixed coefficient table is reused by successive, independently processed profiles. (**b**) One robust-fit iteration, with $d = |e - m_e|$ denoting the absolute deviation from the residual median and $t = 1.345s$ the weighting threshold for residual scale s. (**c**) Sequential formation of eight denominators, followed by extinction calculation and validity checks for the same bins. The cumulative sum is retained between groups.

4. Experimental Evaluation

4.1. Experimental Setup

The lidar was deployed on a rooftop 10 m above ground level on Science Island, Hefei, Anhui, and operated along a horizontal path (Figure 5). A PWD50 visibility sensor (Vaisala Oyj, Vantaa, Finland) was located approximately 1.0 km from the lidar near the observation path.



Figure 5. Experimental setup for near-surface aerosol validation. The LiDAR system is deployed on a building rooftop (10 m AGL) operating in a continuous horizontal sounding mode. A PWD50 forward-scatter visibility sensor is positioned at a range of 1.0 km along the laser line-of-sight, providing an independent visibility-derived reference for the extinction retrieval.

The numerical and timing tests used a measured analog profile acquired with the settings in Table 2. A PWD50 forward-scatter visibility sensor was positioned approximately 1.0 km along the lidar line of sight. The deployment-data analysis converted visibility V to extinction α_V using the Koschmieder relation:

$$\alpha_V = \frac{-\ln \epsilon}{V} \approx \frac{2.996}{V} \tag{8}$$

where $\epsilon = 0.05$ is the contrast threshold used in that conversion. Visibility is expressed in kilometres and α_V in km^{-1}. For the comparison, the lidar extinction was taken at approximately 1.0 km along the observation path, near the PWD50 location. The lidar and PWD50 records were first aligned in time. Lidar extinction values at this location were then averaged within each comparison interval. Each mean was compared with the extinction derived from the corresponding PWD50 visibility measurement.

4.2. Numerical and Field Comparisons

4.2.1. Numerical Agreement

The ARM implementation and a desktop C build of the same mixed-precision code were evaluated using the same measured 4000-bin analog profile and model parameters (Figure 6). The maximum absolute difference over all matched valid range bins was 2.384×10^{-7} km^{-1}, and the validity masks were identical.

Figure 6 shows the profiles and their differences over 0–4 km. The curves overlap, including the local variation shown in the inset. This comparison supports the numerical consistency of the ARM and desktop implementations for the tested profile.

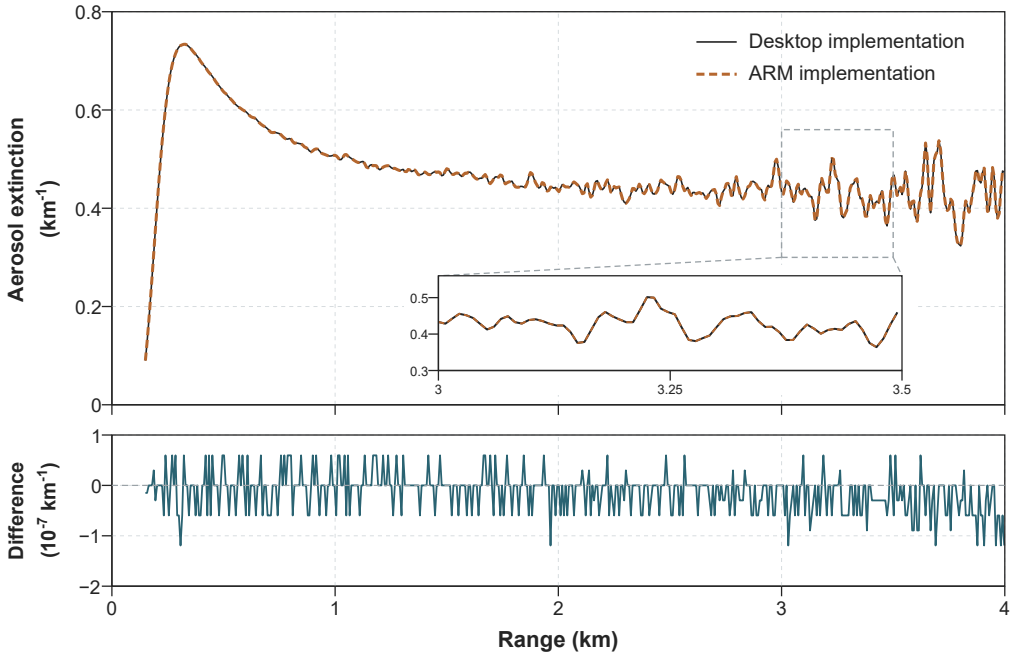


Figure 6. Numerical comparison between the ARM and desktop C implementations of the same mixed-precision retrieval code for one measured analog profile. Extinction profiles and ARM-minus-desktop differences are shown over 0–4 km. The maximum difference reported in the text is evaluated over all matched valid range bins.

4.2.2. Comparison with the Visibility-Derived Reference

Figure 7 compares the lidar and PWD50-derived extinction records over 16 h, from 14:00 on 2 December to 06:00 on 3 December 2025 (UTC+8), using the processing described

in Section 4.1. Both records rise sharply between approximately 18:00 and 19:00, remain elevated during the late evening, and decrease after midnight.

The paired values in Figure 7b follow a similar trend, although the fitted relation departs from the 1:1 line. The instruments sample different atmospheric volumes even near the same location, so local aerosol variability can affect individual pairs. The prescribed lidar ratio and reference boundary may also affect the retrieved extinction [15,16]. We therefore place greater emphasis on the shared temporal changes, while the scatter plot shows the remaining differences between the two records.

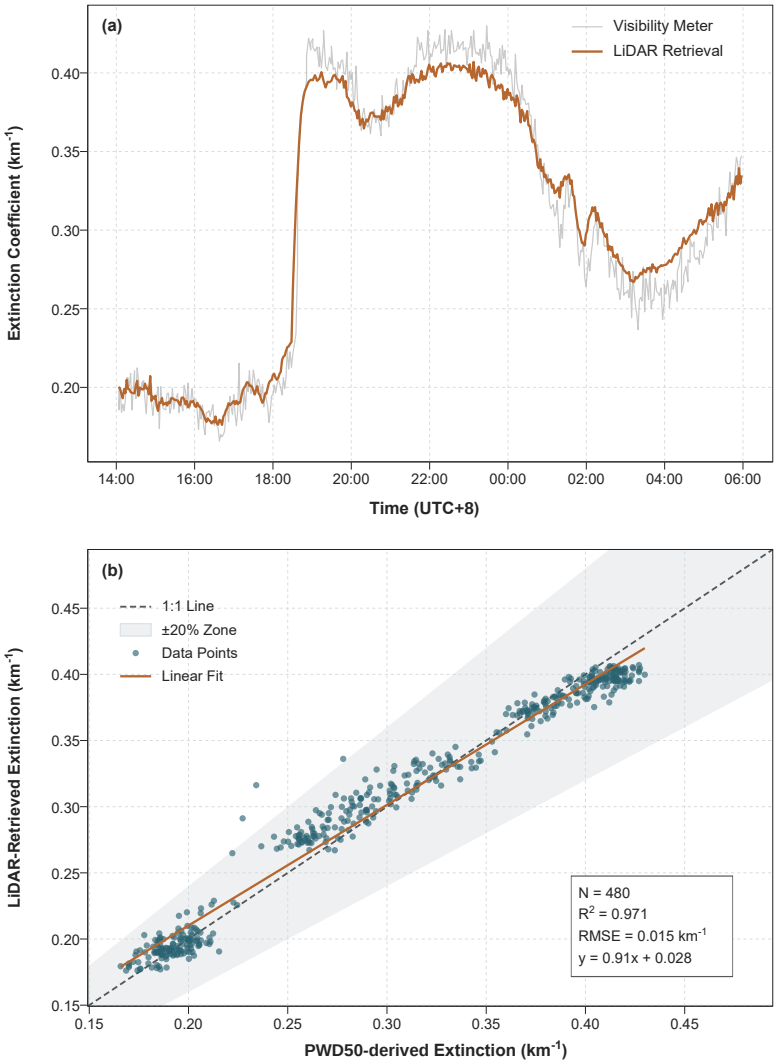


Figure 7. Comparison of the lidar extinction at approximately 1.0 km with PWD50-derived extinction. (**a**) Records over the common observation interval, with time expressed as UTC+8. (**b**) Paired values, the 1:1 line, and the fitted linear relation.

4.3. Processing Time on the ARM Processor

The three implementations were benchmarked on a 667 MHz ARM Cortex-A9 processor integrated in the Xilinx Zynq-7000 SoC (XC7Z020; Xilinx, Inc., San Jose, CA, USA). using Xilinx SDK 2018.3 and GCC 7.3.1 in a standalone environment. They were compiled into the same executable and processed the same measured 4000-bin analog profile. All used `-O3`, hardware floating point, and enabled instruction and data caches; fast-math, floating-point contraction, and link-time optimization were disabled.

The direct C implementation evaluates the normalization terms, including the exponential, separately at each range bin. The conventional C implementation precomputes

composite coefficients and uses loop fusion and unrolling. The optimized implementation combines these changes with the mixed-precision arithmetic, fitting routines, and eight-bin processing described in Section 3.3. The implementations use the same retrieval equations and reference-selection criteria.

Two scopes were timed using the processor timer. Fixed-reference processing included preprocessing, extinction retrieval, and validity checks; the second scope also included reference selection. One-time initialization, profile readout, task scheduling, and data output were outside the timed region. For fixed-reference processing, the reported time is the median of 11 batch averages, each obtained from 20 calls after a warm-up call. For processing with reference selection, it is the median of seven calls. The execution order was rotated between repetitions, and all measurements came from one board run.

With a fixed reference, processing took 1.931 ms for direct C, 0.846 ms for conventional C, and 0.357 ms for the optimized implementation (Figure 8a). When reference selection was included, the corresponding times were 50.00, 48.75, and 12.49 ms (Figure 8b). Coefficient reuse and conventional loop changes therefore reduced the fixed-reference cost substantially but had little effect on the time including reference selection. The additional changes reduced this broader workload, giving a fourfold reduction relative to direct C.

For the optimized implementation, the seven calls including reference selection ranged from 12.4335 to 12.6187 ms, with a mean of 12.4938 ms. The median was 12.4923 ms, reported as 12.49 ms in Figure 8b. These repetitions characterize timing for the selected input.

All three implementations completed the tested computation within the 1 s interval between accumulated profiles. The configured 4000 bins cover a nominal recording range of 30 km, whereas useful returns under the present measurement conditions were confined to ranges below 10 km. Extending this window would mainly add background-dominated bins. The measured times describe algorithm execution; profile readout, task scheduling, and data output were excluded.

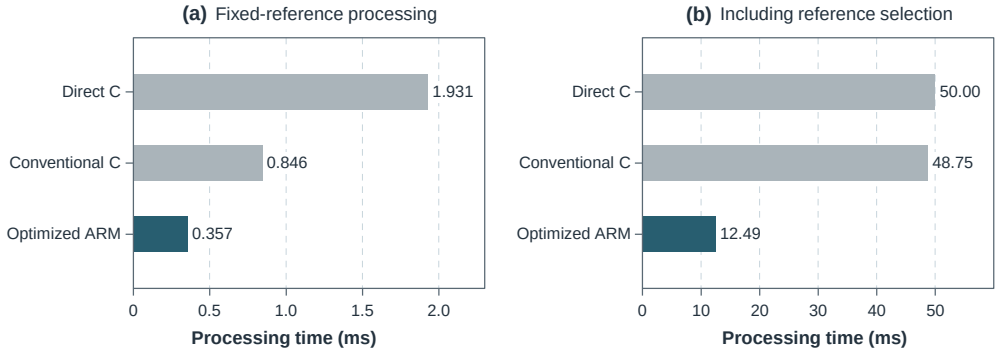


Figure 8. Processing times on the ARM Cortex-A9 for one measured 4000-bin analog profile: (**a**) preprocessing, retrieval, and validity checks with a fixed reference; (**b**) the same processing including reference selection. Bars show median times obtained with the common build settings and timing procedure described in the text.

4.4. Continuous Horizontal Observation

The acquisition–retrieval chain was operated continuously from 18:00 on 6 January to 06:00 on 9 January 2026 (UTC+8). During this 60 h deployment, 216,000 profiles were exported at one profile per second, with no missing profiles in the exported sequence and no observed processing overruns. Figure 9 shows the extinction record over horizontal range and time.

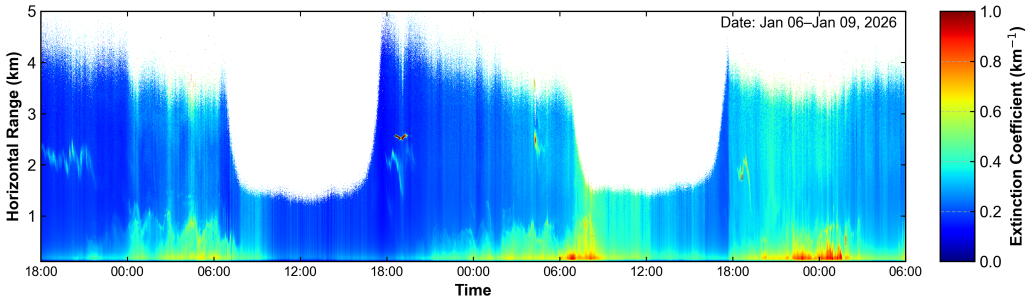


Figure 9. Extinction range–time record from the 60 h horizontal observation, from 18:00 on 6 January to 06:00 on 9 January 2026. All times are local time (UTC+8).

Increased daytime background reduces the SNR at longer ranges. The retrieval algorithm marks bins with SNR below 3 as invalid. For the algorithm output, the maximum valid range is the farthest bin retained by the stated validity criteria in each profile.

During the 60 h deployment, both the displayed range and the retrieved extinction coefficient showed clear day–night variations. The displayed range extended to approximately 4–5 km at night. The extinction coefficient was generally higher at night, particularly from the pre-dawn hours into early morning, indicating reduced visibility. During daytime, lower extinction coefficients indicated better visibility. The acquisition–retrieval chain recorded these variations in successive range-resolved profiles throughout the observation period, demonstrating the capability of the integrated system for sustained atmospheric monitoring.

5. Discussion and Limitations

The system produces extinction profiles within the lidar instrument by assigning pulse-level acquisition to the PL and profile-level retrieval to the ARM. Profile handover and task scheduling connect these stages while acquisition continues.

All three implementations processed the tested profile within the 1 s acquisition interval, so the optimization provides additional time for readout and communication. Reference selection accounts for most of the measured computation time, which explains why the conventional coefficient and loop changes have little effect on the total time. Processing times over a wider range of reference-search workloads remain to be measured.

The retrieved extinction depends on the prescribed lidar ratio and reference boundary. Sensitivity to assumptions relating backscatter and extinction has been examined previously [15]; the present timing and numerical comparisons do not quantify this uncertainty for S_a = 20–70 sr. The slope-derived boundary assumes an approximately homogeneous reference interval along range, as in the slope-method formulation [11]. A plume or sustained backscatter gradient within that interval can bias the boundary even when the fitted signal is smooth. Shin et al. examined reference estimation under heterogeneous horizontal conditions, including the influence of local aerosol sources, and proposed a multi-section approach [16]. Boundary searches based on forward integration provide another option for horizontal measurements [17]. Because reference estimation is performed in the ARM software, a different estimator can be incorporated without changing the PL acquisition logic, although its retrieval performance and processing cost would need to be evaluated.

6. Conclusions

An integrated acquisition and retrieval system was implemented for a 532 nm atmospheric lidar. Coordinated PL acquisition, profile handover, and ARM processing allow extinction retrieval to proceed while subsequent echoes are acquired. For the tested profile, the optimized code took 12.49 ms including reference selection, within the 1 s profile acquisition interval, and produced results consistent with the desktop C implementation.

A 60 h horizontal deployment produced a sequence of range-resolved extinction profiles, demonstrating sustained operation of the acquisition–retrieval chain.

Author Contributions: C.X. provided supervision and resources, including equipment support, and contributed to writing—review and editing. R.G. was responsible for conceptualization, methodology, software development, formal analysis, investigation, data curation, visualization, and writing. J.L. contributed to discussions on the retrieval algorithm. Z.Z. and R.Z. participated in system debugging and testing. All authors have read and agreed to the published version of the manuscript.

Funding: This research received no external funding.

Institutional Review Board Statement: Not applicable.

Informed Consent Statement: Not applicable.

Data Availability Statement: The data supporting the findings of this study are available from the corresponding author upon reasonable request.

Acknowledgments: The authors thank the Anhui Institute of Optics and Fine Mechanics of the Chinese Academy of Sciences for providing the hardware and software platform. The authors used ChatGPT 5.6 sol (OpenAI) to assist with English language editing, including grammar and wording improvements. The authors reviewed and edited the output and take full responsibility for the content of this publication.

Conflicts of Interest: The authors declare no conflicts of interest.

References

1. Pappalardo, G.; Amodeo, A.; Apituley, A.; Comeron, A.; Freudenthaler, V.; Linné, H.; Ansmann, A.; Bösenberg, J.; D'Amico, G.; Mattis, I.; et al. EARLINET: Towards an advanced sustainable European aerosol lidar network. *Atmos. Meas. Tech.* **2014**, *7*, 2389–2409. [CrossRef]
2. Sanchez Barrero, M.F.; Popovici, I.E.; Goloub, P.; Victori, S.; Hu, Q.; Torres, B.; Podvin, T.; Blarel, L.; Dubois, G.; Ducos, F.; et al. Enhancing mobile aerosol monitoring with CE376 dual-wavelength depolarization lidar. *Atmos. Meas. Tech.* **2024**, *17*, 3121–3146. [CrossRef]
3. González, Y.; Sánchez-Barrero, M.F.; Popovici, I.; Barreto, Á.; Victori, S.; Welton, E.J.; García, R.D.; Sicilia, P.G.; Almansa, F.A.; Torres, C.; et al. Compact dual-wavelength depolarization lidar for aerosol characterization over the subtropical North Atlantic. *Atmos. Meas. Tech.* **2025**, *18*, 1885–1908. [CrossRef]
4. Li, Q.; Xin, Y.; Chen, C.; Li, Y.; Jiang, Y.; Song, W. Development and observation of a three-dimensional scanning coaxial Mie lidar for dynamic monitoring of near-surface aerosol plumes. *Front. Earth Sci.* **2024**, *12*, 1430178. [CrossRef]
5. Cheng, L.; Xie, C.; Zhao, M.; Li, L.; Yang, H.; Fang, Z.; Chen, J.; Liu, D.; Wang, Y. Design of Lidar Data Acquisition and Control System in High Repetition Rate and Photon-Counting Mode: Providing Testing for Space-Borne Lidar. *Sensors* **2022**, *22*, 3706. [CrossRef] [PubMed]
6. Cheng, L.; Xie, C. An Integrated Off-Line Echo Signal Acquisition System Implemented in SoC-FPGA for High Repetition Rate Lidar. *Electronics* **2023**, *12*, 2331. [CrossRef]
7. Chouza, F.; Leblanc, T.; Wang, P.; Brown, S.S.; Zuraski, K.; Chace, W.; Womack, C.C.; Peischl, J.; Hair, J.; Shingler, T.; et al. The Small Mobile Ozone Lidar (SMOL): Instrument description and first results. *Atmos. Meas. Tech.* **2025**, *18*, 405–419. [CrossRef]
8. Liu, Q.; Zhu, W.; Jin, X.; Qing, C. Real-Time Synchronous Acquisition and Processing of Signal in Coherent Doppler Wind Lidar Using FPGA. *Remote Sens.* **2023**, *15*, 5673. [CrossRef]
9. Jackson, R.C.; Raut, B.A.; Dematties, D.; Collis, S.M.; Ferrier, N.; Beckman, P.; Sankaran, R.; Kim, Y.; Park, S.; Shahkarami, S.; et al. ARMing the Edge: Designing Edge Computing–Capable Machine Learning Algorithms to Target ARM Doppler Lidar Processing. *Artif. Intell. Earth Syst.* **2023**, *2*, e220062. [CrossRef]
10. Kim, Y.H.; Lee, J.; Gi, S.g.; Lee, S.; Cho, J. A Light-weight Asymmetric Multi-Processing FPGA Architecture for Real-time High-resolution LiDAR. *J. Sens. Sci. Technol.* **2025**, *34*, 660–667. [CrossRef]
11. Kunz, G.J.; de Leeuw, G. Inversion of lidar signals with the slope method. *Appl. Opt.* **1993**, *32*, 3249–3256. [CrossRef] [PubMed]
12. Mei, L.; Guan, P.; Yang, Y.; Kong, Z. Atmospheric extinction coefficient retrieval and validation for the single-band Mie-scattering Scheimpflug lidar technique. *Opt. Express* **2017**, *25*, A628–A638. [CrossRef] [PubMed]
13. Fernald, F.G. Analysis of atmospheric lidar observations: Some comments. *Appl. Opt.* **1984**, *23*, 652–653. [CrossRef] [PubMed]
14. Weitkamp, C. (Ed.) *Lidar: Range-Resolved Optical Remote Sensing of the Atmosphere*; Springer Series in Optical Sciences; Springer: New York, NY, USA, 2005; Volume 102. [CrossRef]

15. Hughes, H.G.; Ferguson, J.A.; Stephens, D.H. Sensitivity of a lidar inversion algorithm to parameters relating atmospheric backscatter and extinction. *Appl. Opt.* **1985**, *24*, 1609–1613. [CrossRef] [PubMed]
16. Shin, J.; Kim, G.; Kim, D.; Tesche, M.; Park, G.; Noh, Y. Multi-section reference value for the analysis of horizontally scanning aerosol lidar observations. *Atmos. Meas. Tech.* **2024**, *17*, 397–406. [CrossRef]
17. Zhao, M.; Chen, J.; Zheng, J.; Meng, D.; Yang, J.; Zhuang, P.; Yang, K.; Wang, C.; Xie, C. A Novel Method for Boundary Value Determination in the Fernald Inversion for Horizontal Lidar Measurements. *Photonics* **2026**, *13*, 162. [CrossRef]

Disclaimer/Publisher's Note: The statements, opinions and data contained in all publications are solely those of the individual author(s) and contributor(s) and not of MDPI and/or the editor(s). MDPI and/or the editor(s) disclaim responsibility for any injury to people or property resulting from any ideas, methods, instructions or products referred to in the content.